Tear resistance of a square-wave joint: experiment versus cohesive zone model

Kevin Maloney and Norman Fleck*

Cambridge University Engineering Department, Trumpington Street,

Cambridge, CB2 1PZ, UK

Abstract

The load versus displacement response of a double-cantilever beam (DCB) adhesive joint is measured for two interface geometries: a planar interface and a non-planar "square-wave" interface. Joints with a square-wave interface are stronger and tougher than planar joints of equal adhesive layer thickness provided the square-wave amplitude is sufficiently large. Computed tomography (CT) imaging is used to examine the failure morphology of DCB specimens with planar interfaces, and optical fractography is used to observe the failure mechanisms for DCB specimens with square-wave joints of fixed wavelength and selected amplitude; in all cases, the failure mode is similar to those of tensile, square-wave, butt joints. The finite element method is used to predict the cracking response of the DCB adhesive joint. To do so, the adhesive layer is idealised as a plane of cohesive elements with a normal traction versus separation response, as measured independently from square-wave butt joint specimens. Satisfactory agreement exists between the predicted and observed DCB response for all interface geometries, provided the reduction in DCB bending stiffness, arising as a consequence of the square-wave interface geometry, is taken into account.

*Corresponding author: naf1@eng.cam.ac.uk

1. Introduction

Commonly, adhesive joints are stronger and tougher under shear loading (such as a lap joint) configuration, than under tensile loading (such as a butt joint). This suggests that a strategy

1

for increasing the peel strength and peel toughness of a joint is to inter-digitate the two substrates, and thereby exploit the high strength and toughness associated with a lap-joint configuration, see for example Maloney and Fleck (2017).

The present study builds on the promising studies on micro-patterned adhesive joints by Matsuzaki and co-workers (Matsukaki and Suzuki, 2010; Suzuki et al., 2013; Hikosaka et al., 2013; Yukimoto et al., 2014; Suzuki et al., 2015) and on the work of Kim et al. (2010). These studies make use of an in-mold surface modification method whereby a corrugated molding tool is pressed against a low-viscosity matrix during curing of a composite, and the patterns are transferred by demolding at low temperature. The wavelength and amplitude of the pattern is typically on the order of 10 μm, and an elevation in the butt joint strength, macroscopic mode I toughness of a double cantilever beam (DCB) specimen, and macroscopic mode II toughness of an end-notch flexure (ENF) specimen increase with the amplitude of the pattern (typically by a factor of 50% in strength and 100% in toughness). More recently, Cordisco et al (2016) investigated sinusoidal DCBs of amplitude A and wavelength λ with A/λ in the range 1/4 to 1/2; they found that the peak load increased with A/λ and concluded that patterned adhesive joints can be substantially tougher than joints with no pattern. Maloney and Fleck (2017) conducted tensile tests on butt joints of square-wave configuration, and observed that the measured tensile strength and energy absorption increase with amplitude A.

Suzuki et al. (2013, 2015) have modelled the mode I response of a DCB specimen with a micro-patterned joint by placing cohesive zones along the profiled interface of the joint and also within the adhesive. An elastic-brittle analysis sufficed, with no dissipation in the adhesive layer, as the epoxy adhesive was of low toughness. The present study explores a different class of adhesive (elastomeric rather than untoughened epoxy), and on a different length scale of patterning (millimetre scale rather than micron scale).

Crack advance within a joint is commonly modelled by a cohesive zone approach, with the traction versus displacement response of the cohesive zone sensitive to the thickness of the adhesive layer (Yang et al. 1999; Gustafson and Waas, 2009; Stigh et al., 2010). Cohesive zone modelling (CZM) has become a popular tool for predicting the fracture response of adhesive joints (Li et al., 2005; Tvergaard and Hutchinson, 1996, 1994, 1992). The CZM approach can capture the linear-elastic fracture mechanics (LEFM) limit whereby the zone of inelasticity is much less than that of leading structural dimensions such as crack length or ligament size. It can also capture large-scale bridging where LEFM fails, see for example Elices et al. (2002), Yang and Cox (2005) and Alfano et al. (2009).

Commonly, the traction versus separation (T-δ) response of the "cohesive zone" is defined by two parameters such as the cohesive strength and work of separation, or cohesive strength and critical separation (Blackman et al., 2003; Alfano, 2006; Campilho et al., 2013). Cohesive zones have been used to model crack initiation (Mohammed and Liechti, 2000), but they are more commonly used to model the growth of a crack (Elices et al., 2002). We note that the CZM represents both the process zone ahead of the crack and the bridging zone in the wake of the crack, and the CZM length can vary from nanometres to millimetres (Shet and Chandra, 2002; Stigh et al., 2010; Zhu et al., 2009).

There is scope for choosing the appropriate level of sophistication in a cohesive zone model, depending upon the research question to be addressed. For example, the role of mode mix on the fracture strength and toughness can be analysed by suitable modification to the traction versus separation law across the cohesive zone, see for example Yang and Thouless (2001). The role of plastic yielding in the adherends has been addressed by Ferracin et al. (2003) for the wedge-peel test and by Georgiou et al. (2003) for the peel test, with the deformation and fracture response of the adhesive idealised by a cohesive zone. This pragmatic approach requires a calibration of the bondline toughness as a function of the thickness of the adhesive layer. In contrast, Pardoen et al. (2005) model explicitly plastic deformation within both the adherends and the adhesive, but idealise the fracture process zone by a cohesive zone law; in this manner, the role of constraint effects and thickness of adhesive layer can be modelled. However, the details of the crack tip failure mechanism are not interrogated explicitly by this approach; to do so would require a detailed constitutive model for microvoid growth or crazing within the fracture process zone, along with a representative material length scale in order to predict the macroscopic toughness. Nevertheless, the use of a cohesive zone embedded within an elasto-plastic adhesive layer and outer elasto-plastic adherends is a useful predictive tool, and has been validated for the peel test by Martiny et al. (2008), and for the tapered double cantilever beam by Cooper et al. (2012). Recently, the importance of rate effects in the failure of rubber-toughened epoxies has been highlighted by Karac et al (2011) by making use of a crack velocity dependent cohesive zone law to predict the load versus displacement response of a tapered double cantilever beam.

1.1 Determination of the Cohesive Zone Law

The central task of implementing a cohesive zone model is a determination of the traction versus separation (T-δ) law, or "cohesive law", to define the response of cohesive elements (Park and Paulino, 2013; Stigh et al., 2010; Salomonsson and Andersson, 2008). Most

methods assume a simple shape for the traction-separation law and attempt to match the results of a finite element simulation to experimental measurements by varying the parameters of the cohesive law such as the peak traction or energy dissipation. When adequate agreement is achieved between simulation and experiment, it is assumed that the correct cohesive parameters have been deduced (Yang and Thouless, 2001).

There exist two main methods for measuring a Mode I cohesive law directly from experimental results. The first makes use of the measured J-integral for a crack in a double-cantilever beam specimen, and a simultaneous measurement of the crack tip opening displacement (and crack tip opening angle). The traction exerted by the cohesive layer is the derivative of the J-integral with respect to the crack tip opening displacement. This method has been used by several researchers to derive empirically-based cohesive laws (Desai et al., 2015; Sørensen, 2002; Stigh et al., 2010; Zhu et al., 2009) and generally provides accurate predictions of the response of a cracked specimen.

The second method is more straightforward, but there are only limited studies to explore its validity. The Mode I cohesive law is assumed to equal the T-δ response of a tensile specimen so-chosen to represent a thin ligament ahead of the crack. Ivankovic et al. (2004) pursued this strategy to model the response of cracked three-point-bend polyethylene specimens with mixed success. They extended their model by including rate-dependence in the cohesive law and thereby achieved satisfactory predictions. They recognized the shortcomings of this approach and proposed the development of a physical material model which could describe the local fracture process by a T-δ response which depends on rate, constraint and temperature.

1.2 Scope of the Present Study

In this study, the load versus displacement response of a double-cantilever beam (DCB) specimen with a square-wave interface geometry is explored as a function of square-wave amplitude. The observed failure mechanisms of square-wave DCB specimens are compared to those observed for tensile butt joints with square-wave interfaces as presented in a previous study (Maloney and Fleck, 2017).

A finite element model is used to predict the response of double-cantilever beams with either a planar interface or a square-wave interface. The adhesive layer is represented by cohesive elements with a traction versus separation response as specified by the measured tensile response of a butt joint specimen with the same micro-architecture (planar or square-wave).

The accuracy of the finite element model is evaluated by comparing the predicted load versus displacement response to the measurements. Additionally, the accuracy of a *J*-integral method for predicting the load versus displacement response of DCB joints with planar interfaces is confirmed in the appendix.

2. Materials and Methods

2.1 Experimental Methods

The adhesive joints comprised a two-part, room-temperature and moisture-curing silyl-modified polymer (SMP) adhesive[1] sandwiched between aluminium alloy 6082-T651 substrates. The adhesive contains filler particles on a scale of 10 μm to control its viscosity in an un-cured state. The double-cantilever beam (DCB) joint is characterised by arms of height $H = 25.4$ mm, beam lengths l and L of 25.4 mm and 228.6 mm, respectively, and a starter crack of length $a_o = 30$ mm, see

Figure 1(a). The square-wave interface geometry was presented in a previous study (Maloney and Fleck, 2017). It is characterised by five parameters as defined in

Figure 1(b). The amplitude A ranges from 0 mm (corresponding to a planar interface) to 20 mm, while the magnitude of wavelength λ, adhesive thickness parameters t and s, and depth (into page) B are fixed at $\lambda = 28$ mm, $t = s = 1.1$ mm, and $B = 12.8$ mm. The pattern wavelength and layer thickness were chosen within the practical range for the manufacturing and test methods adopted. Suitably-shaped substrates were water-jet cut to within a dimensional tolerance of 0.1 mm.

2.1.1 Specimen Preparation

Roughening of the substrates was accomplished by manual polishing using 60 grit emery paper; the surfaces were then cleaned and degreased by wiping with acetone. The adhesive was applied in accordance with the manufacturer's recommendations. A manual applicator gun was used with a static-mixing nozzle. A quantity of adhesive was initially discarded to ensure that both components were flowing freely and to remove any bubbles which may have

---

[1] Sabatack Fast, produced by SABA Dinxperlo BV, Industriestraat 3, 7091 DC Dinxperlo, Netherlands.

accumulated in the component tubes. The adhesive layer thickness t was adjusted by shims prior to infiltration of the gap by the adhesive. All specimens were cured in ambient air for one week at room temperature, and G-clamps were used to prevent relative movement of the substrates. A starter crack was generated in all specimens by making use of fresh razor blades: the razor blade was broached to a depth of 5mm, for to give an initial crack length of 30mm. Additionally, the uniaxial response of the SMP adhesive was measured by casting a dogbone specimen from the adhesive, of gauge length 20 mm and square cross-section 6.5 mm x 6.5 mm.

2.1.2   Test Procedure

Mechanical tests were conducted using a screw-driven test machine, as follows.

(i)   Uniaxial tension tests on dogbone specimens of SMP adhesive were performed in accordance with ASTM D638-14 at machine displacement rates in the range 0.01 mm s^{-1} to 1000 mm s^{-1} to characterise the viscoelastic nature of the adhesive.

(ii)   At least three DCB specimens of each joint geometry were tested, and the scatter was expressed in terms of the standard deviation of each set of specimens. The tensile load on each specimen was measured by the load cell of the test machine, while the displacement was measured by the test machine and by a laser extensometer[2]. The machine-measured displacement was corrected for the compliance of the test machine and was used to corroborate the measurements of the laser extensometer, which were used to generate the results presented in the current study. The tests on double-cantilever beam (DCB) joints were conducted at a displacement rate of 0.007 mm/s, and photographs[3] were collected at a frame rate of 0.5 frames per second to monitor crack growth. Additionally, tests on the DCB specimens with planar joints were interrupted and the specimens were placed in a 3D computed tomography (CT) machine[4] in order to observe the formation of voids within the adhesive layer ahead of the crack tip. The CT scan took 30 minutes, and there was little change in the opening profile of the specimen during the scan due to the presence of the wedge. The main purpose of the CT tomography was to examine the process zone within the adhesive joint for the planar specimen. It proved difficult to obtain high resolution images of the square wave joints, and to the study was limited to CT tomography of the planar joint.

---

[2] Electronic Instrument Research Laser Extensometer, Model LE-05.
[3] PixeLINK PL-B776U Aptina MT9T001 Machine Vision Camera.
[4] Nikon X-TEK 3D CT Machine (Model XT 225ST).

(iii) The tensile traction versus opening displacement of square-wave butt joints were also determined using a machine displacement rate of 8 x 10^{-3} mm·s^{-1} corresponding to a normalised displacement rate $\dot{\delta}/t$ of approximately 7 x 10^{-3} s^{-1}. At least three specimens of each joint geometry were tested.

3. Results and Discussion

3.1 Bulk Properties of Elastomeric Adhesive

The uniaxial tensile stress versus strain response of the SMP adhesive is given in Figure 2 for three values of nominal strain rate (3 x 10^{-3} s^{-1}, 3 x 10^{-1} s^{-1} and 30 s^{-1}). Both the nominal and true stress versus strain responses are plotted. Note that the shape of the stress versus strain response is independent of strain rate but the strain to failure (and associated tensile strength) is mildly sensitive to strain rate. As the strain rate is increased from 3 x 10^{-3} s^{-1} to 30 s^{-1}, the nominal failure strength, that is, the ultimate tensile strength UTS, increases from 2.5 MPa to 3.6 MPa and the true (logarithmic) strain to failure increases from 0.95 to 1.42, while the Young's modulus E is almost constant at 2.5 ± 0.2 MPa.

3.2 Planar Joints

The load P versus displacement u response of a double-cantilever beam (DCB) with a planar adhesive layer ($A = 0$ mm) is shown in Figure 3(a). No plastic deformation of the aluminium substrates was observed, and this was confirmed by load-unload tests. This is consistent with the relative strengths of the two solids: the aluminium alloy has a yield strength of 250MPa whereas the SMP adhesive has a UTS of 2 MPa. The non-linear behaviour observed in the initial portion of the DCB load versus displacement response can be traced to the non-linear tensile response of dogbone specimens made from the bulk adhesive, recall Figure 2.

Crack growth in the DCB specimens with a planar adhesive layer begins shortly after peak load, and crack advance leads to a decreasing load. CT images of the mid-plane of the adhesive layer are shown in Figure 3(b) at the following snapshots in time, upon interruption of the testing: (i) initial state, (ii) prior to peak load and (iii) after a crack advance of 42 mm. Recall that the DCB specimens are of thickness B=12.8mm (in the z-direction), which can be used as a length scale in interpreting the fracture surfaces of Figure 3(b). The leftmost end of the images in Figure 3(b) are aligned with the initial crack tip (at a pre-crack length of

7

30mm), while the rightmost end of the images are 100mm ahead of the initial crack tip. (Recall that the specimen ligament is of width 200mm ahead of the initial crack tip).

In the initial state, only a few small voids are visible. At the loading point (ii) of the P versus u curve, microvoids exist within the adhesive, but the voids are too small to be resolved by the CT machine. (Large voids are visible as white circles, while microvoiding is dispersed throughout as grey scale.) Since the effective density of the adhesive is reduced by the presence of the microvoids, the image becomes lighter, as shown in the light grey region ahead of the crack tip in (ii) of Figure 3(b). The SMP adhesive can sustain a large amount of voiding prior to void coalescence, in contrast to an epoxy, for example. Thus, voids can exist far ahead of the crack tip.

Beyond peak load, at point (iii), a new zone of microvoids (light in appearance) is present ahead of the current crack tip, along with a low volume fraction of larger voids. The lighter zone in (iii) is a developing damage zone that progressively fails to give rise to crack advance. Note that the voided zone extends beyond the rightmost end of the image in (iii) of Figure 3(b). At this stage of loading, a few larger voids have also nucleated and grown ahead of the grey-zone of microvoids. A representative fracture surface is shown in Figure 3(c): it reveals that the microvoiding occurs from filler particles within the adhesive.

The combination of microvoids and occasional larger voids has been observed in the previous study of Maloney and Fleck (2017) in butt joint tests on this adhesive. The similarity in the observed progression of damage for the DCB geometry and for the butt joint geometry supports the use of the measured traction versus opening response of the butt joint in calibrating the cohesive zone model for the DCB tests.

3.3 Square-wave Joints

The load P versus displacement u responses of a planar DCB joint ($A = 0$ mm) and three square-wave DCB joints with amplitudes $A = 2.5$ mm, 10 mm and 20 mm are presented in Figure 4(a). The adhesive layer thickness t is equal to 1.1 mm for all joints. The peak load of the joint with amplitude $A = 2.5$ mm is 1610 N, and this is 13% less than that of the planar DCB joint ($A = 0$ mm). Also, the small-amplitude square-wave joint dissipates 25% less energy than that of the planar joint. However, upon increasing the square-wave amplitude A to above 2.5 mm, the peak load and dissipated energy increase monotonically with increasing A.

The tensile traction versus separation (T-δ) response of the "square-wave" adhesive butt joint has also been measured as a function of square-wave amplitude A, including the limit of the planar adhesive joint, with the adhesive layer thickness fixed at 1.1mm. The traction is defined as the tensile load divided by the projected cross-sectional area of the joint normal to the loading direction; the separation δ is the tensile relative opening displacement across the adhesive joint, as measured by a laser extensometer. The traction T versus separation δ responses of a planar butt joint and three square-wave butt joints with amplitudes A = 2.5 mm, 10 mm and 20 mm are presented in Figure 4(b). It is observed from repeat tests that the average peak traction increases monotonically from 2.2 MPa to 2.4 MPa for joints with square-wave amplitudes in the range 0 mm $\leq A \leq$ 10 mm, and jumps to 2.9 MPa for the large-amplitude joint. The double-peak in the T-δ curve for A=20mm in Figure 4(b) is discussed in detail in Maloney and Fleck (2017). The double peak is due to the fact that the square wave has 2 failure modes: the tensile zones at the top and bottom of the square wave fail in the manner of a tensile butt joint, and give the first load peak. The sides of the square wave are loaded in shear in the manner of a lap joint, and fail independently at a larger displacement across the joint.

Recall that the ultimate tensile strength UTS of the dogbone specimens is 2.3MPa at a comparable strain rate to that of the square wave butt joints, compare Figures 2 and 4(b). Also the nominal failure strain of the dogbone specimens is on the order of 1.6. The planar butt joint (A=0) has a peak strength of 2.3 MPa, and a failure strain δ /t =2.0, which are of similar magnitude to those of the tensile dogbone specimens. However, the degree of elastic constraint is significantly higher in the butt joint specimens.

The energy dissipated Γ is calculated as the area under the T-δ curve. The value for Γ is based on the projected area of the square-wave, that is the side faces of the square-wave are neglected. This is consistent with the definition of traction T per unit projected area of the joint. The energy dissipated Γ by double-cantilever beam joints and tensile butt joints is presented in Figure 4(c) as a function of square-wave amplitude A. The cross-sectional area of the DCB arms (ahead of the initial crack tip) was used in the calculation of the energy dissipated per unit area.

For both types of specimen, the average dissipated energy initially decreases from values for planar specimens (A = 0 mm) to those for square-waves of amplitude A = 2.5 mm. This is followed by an increase in dissipated energy for square-wave joints of amplitude A = 10 mm and A = 20 mm to levels that exceed those for planar specimens. There is good agreement between the dissipated energy for butt joints and DCB joints for all square-wave amplitudes.

For the amplitude range $2.5 \leq A \leq 20$ mm, the increase in dissipated energy follows an approximately linear trend, similar to the findings of Zavattieri et al. (2007) and Cordisco et al. (2016) for the Mode I toughness of adhesively-bonded sinusoidal interfaces.

The observed failure sequence of a DCB joint with square-wave amplitude $A = 20$ mm is presented in Figure 5. The sequence of debonding in the adhesive layer ahead of the crack tip is compared to the failure sequence of a tensile butt joint from Maloney and Fleck (2017). Consider an unstrained region of the interface ahead of the crack tip. As the adhesive layer undergoes tensile separation, debonding occurs at the internal corners of the square-wave interface, see image (i). As the load-line displacement increases, the voids at each corner expand (image (ii)) and the tensile regions eventually fail, see image (iii). Subsequently, cracks are initiated along each edge of the shear region and experience stable growth under increasing displacement (iv). Finally, opposing shear surfaces fail (see image (v)) and separate from each other. The point when the adhesive in each shear region fails is not obvious, as they continue to bear load in the form of friction between the failed surfaces. The observed failure sequences for all DCB square-wave joints are similar to those observed for butt joints of the same interface geometries.

We conclude that square-wave interfaces only provide mechanical benefits (i.e. higher peak load, greater energy dissipation), in the DCB joint and in the butt joint configuration, when the square-wave amplitude A is sufficiently large. Specimens of small amplitude ($A = 2.5$ mm) fail at a comparable peak load but dissipate slightly less energy than planar joints of the same adhesive layer thickness: only stages (i) to (iii) in the failure sequence of Figure 5 are observed for the small-amplitude square-wave interface, as shear regions fail concurrently with tensile regions. These specimens of small amplitude square-wave possess stress rasers at the corners thereby promoting void nucleation and growth. However, it is somewhat surprising that these specimens are not tougher than the DCB specimens with planar joint in view of the fact that the shear zones of the square –wave act in the manner of a tough lap joint compares to the tensile butt-joint facets of the square wave. For specimens of large square-wave amplitude ($A = 20$ mm), a substantial increase in dissipated energy over joints with planar interfaces ($A = 0$ mm) is attributed to the presence of friction between failed shear surfaces, i.e. a pull-out force or the presence of "mechanical interlocking," as observed in tensile specimens of the same interface geometry in a previous study (Maloney and Fleck, 2017).

4. Numerical Methods

Finite element simulations were performed with the implicit solver of ABAQUS (version 6.12-2). The two-dimensional finite element model consisted of two rectangular elastic substrates joined by a thin cohesive layer (of negligible thickness $t_{cz} = 0.1$ mm as the intent is to mimic a traction-separation law across the adhesive joint). The finite element simulation demands a finite thickness of cohesive zone element for its implementation It is emphasised that both the square-wave DCB specimens and DCB specimens with a planar adhesive joint are modelled as planar specimens, but with a cohesive zone of traction-separation law that has been measured from tests on a butt joint of identical joint architecture. The cohesive zone law for the square-wave joint is meant to capture the average traction-separation law associated with several failure events averaged over the wavelength of the square wave. This is a reasonable approach provided the process zone length in the DCB specimens exceeds the wavelength of the square wave. This is clearly the case, recall Figure 5.

All double-cantilever beam joints were modelled with the same finite element mesh, and the traction T versus separation δ response of the cohesive elements was used to model the square wave topologies. The aluminium alloy substrates of the DCB joint were treated as linear elastic and isotropic, with a Young's modulus $E = 70$ GPa and a Poisson ratio $v = 0.33$. The substrates were meshed with 4-node plane-strain reduced-integration quadrilateral elements (CPE4R).

Both the square-wave and planar adhesive layers were idealised by a planar cohesive zone (of thickness one element), and was meshed by 4-node cohesive elements (COH2D4). The cohesive elements for the square wave and planar joints were defined by a normal traction versus separation response with three parameters: a normal stiffness K, a critical traction T_0 indicating the onset of damage, and a damage variable $D(\delta)$ which describes the evolution of damage as the cohesive element undergoes displacement δ.

A representative cohesive law is presented in Figure 6. A maximum nominal stress-based damage criterion is used such that damage is initiated when a critical traction T_0 is reached. The normal traction exerted on the interface by each cohesive element is calculated as

$$T = \begin{cases} K\delta & \delta \leq T_0/K \\ [1 - D(\delta)]K\delta & \delta > T_0/K \end{cases} \tag{1}$$

where the initial stiffness K and critical traction T_0 are measured values for each of the tensile butt joints of identical micro-architecture to that of the DCB specimens. These values

are listed in Table 1. The cohesive zone laws for the planar joint and square wave joint are taken directly from the load versus displacement response of the tensile butt joints. Consequently, the initial stiffness K is measured and is geometry dependent.

The damage variable D is closely linked to the secant modulus: D evolves from an initial value of zero to a final value of unity, indicating failure of a cohesive element, as the displacement δ increases such that the numerically-constructed curve matches the experimental response. D is defined as follows:

(i) damage does not initiate ($D = 0$) under compressive traction ($T < 0$);

(ii) damage also does not initiate ($D = 0$) for tensile traction less than or equal to the critical traction ($T \leq T_0$); and

(iii) for tensile traction $T > T_0$, $D(\delta)$ evolves in accordance with Eqn. (1) in order to replicate the measured response of the tensile butt joint specimen.

$D(\delta)$ was specified at no less than thirty values of δ for each cohesive law and introduced into the finite element simulation in tabular form. For intermediate values of δ, the finite element solver used linear interpolation to determine the value of the damage variable D from adjacent data points.

5. Predictions by the Finite Element Method

The finite element method is used to predict the response of planar and square-wave DCB joints by a suitable choice of the traction T versus separation δ response of the cohesive elements. The T-δ responses of cohesive elements are constructed from the measured response of tensile butt joints as presented in Figure 4(b).

The predicted load P versus displacement u responses of the finite element model for a planar DCB joint ($A = 0$ mm) and for three square-wave DCB joints of amplitude $A = 2.5$ mm, 10 mm and 20 mm are compared with the measured responses in Figure 7(a). Satisfactory agreement is observed between model and experiment for the planar case and for the small-amplitude ($A = 2.5$ mm) case. The finite element model underpredicts the peak load of the medium-amplitude ($A = 10$ mm) square-wave joint, although the difference is on the order of the scatter for these specimens. The model overpredicts the peak load of the large amplitude ($A = 20$ mm) square-wave joint, and only approximately predicts the shape of the P-u curve for the two square-wave joints of A equal to 10 mm and 20 mm.

We note that the bending stiffness of a cantilever beam with square-wave interface geometry may be significantly less than that of a uniform rectangular beam as adopted implicitly within the finite element model. Our modelling approach so far assumes that each substrate of the DCB joint is modelled as a planar substrate of height H= 25.4 mm. This assumption is an approximation particularly for the large-amplitude square-wave DCB joint: although the average thickness of each substrate equals 25.4 mm, the elastic bending stiffness of the beam is sensitive to the distribution of beam height as dictated by beam theory. Note that, for the choice $A = 20$ mm, the height of the beam varies from 15.4 mm to 35.4mm. Consequently, the effective beam stiffness in these specimens is substantially lower than that assumed in the finite element simulations and this discrepancy contributes to the mismatch between the results of the cohesive zone model and experimental curves.

To address this, the accuracy of the finite element model was improved by assuming an effective beam height H_{eq} in the arms of the DCB specimens such that the bending stiffness of the effective beam equals the average bending stiffness of a cantilever beam with square-wave profile. To achieve this, each arm of the DCB beam was idealised by a single wavelength of square-wave geometry and this arm was subjected to a uniform bending moment at each end in a finite element simulation. The relative rotation of the two ends of the unit cell was determined, and upon dividing this rotation by the length of the unit cell, the average curvature along the length was determined, thereby giving the effective bending stiffness. The equivalent beam height H_{eq} is the height of uniform beam that possesses the same effective bending stiffness as that of the above simulation. This method was used to obtain the equivalent height for substrates of uniform height corresponding to square wave joints of height $A = 2.5, 10$ and 20 mm. Finite element simulations were then performed on DCB specimens of this equivalent height, and results are compared with the measured responses in Figure 7(a). The agreement with the measurements is improved, compare Figures 7(a) and (b).

The slightly higher residual deviation in load at the tail end of the tests in Figure 7(b) can be ascribed to slightly larger interlocking and friction in the DCB specimens as a result of slight tilting compared to the butt joint tests (as used to calibrate the cohesive zone model), particularly at large amplitude A. It is appreciated that the butt joint will not deliver an accurate traction versus separation law for use in finite element predictions of the DCB response when the ratio of amplitude A to adhesive layer thickness s is high, by the following argument. Tilting of the mating arms of the DCB specimen will lead to inter-locking at high A/s and thereby to increased dissipation compared to the butt joint specimens. Consequently,

the load versus displacement response of the DCB specimens will exceed the finite element prediction at high A/s.

6. Concluding Remarks

Crack growth in double-cantilever beam (DCB) joints with planar and non-planar interface geometries has been measured and predicted for aluminium alloy 6082-T651 substrates and a silyl-modified polymer (SMP) adhesive layer. Load versus displacement responses were measured and the observed failure mechanisms have been determined. The planar DCB joints fail by the growth of voids ahead of the crack tip. Square-wave interface geometries of amplitude A = 2.5, 10 and 20 mm failed by void nucleation at the internal corners of the square-wave interface, followed by void growth and coalescence in the portions of the joint that undergo predominantly tensile loading. Failure of the square-wave joint also entails the growth of cracks from the corners of the joint along the regions of predominantly shear loading. As the amplitude A of the joint increases, the proportion of load carried by the shear regions of the joint increases and the joint switches in character from that of a butt joint to that of a lap joint. The magnitude of energy absorbed in the square-wave joint of the DCB specimens increases with increasing A, with the caveat that the square-wave joint of small amplitude A = 2.5 mm is slightly less tough than that of the planar joint; this is attributed to the presence of the sharp corners in the square-wave joint which leads to early void nucleation.

For all interface geometries (both planar and square-wave), the observed failure sequence of DCB joints is similar to the failure sequence of tensile butt joints as presented in a previous study (Maloney and Fleck, 2017). Furthermore, the energy dissipated by DCB joints, per unit (projected) area, is in close agreement to that in tensile butt joints for all interface geometries.

A cohesive zone model is able to predict the load versus displacement responses of double-cantilever beam joints with planar and square-wave interface geometries. In each case, the cohesive zone mimics the tensile response of the adhesive layer, and the cohesive elements are calibrated by the observed response of a butt joint specimen of identical topology (i.e. square-wave, with same value of amplitude A). Satisfactory results are achieved for all joints when the stiffness of the modelled beams is adjusted to match the stiffness of the profiled beams.

The approach adopted herein addresses the following question: can the tensile traction versus separation response of a tensile butt joint of square-wave architecture be used to predict the

progressive cracking response of a DCB specimen of identical joint architecture? It is not immediately obvious that this will be the case. The critical ratio to consider is the length of the process zone in the DCB specimen compared to the square-wave wavelength. When this ratio is large (as it is in the present study), then it is expected that the current approach will be satisfactory. However, when this ratio of length scales is not large, then it is anticipated that the failure sequence in the DCB specimen may involve void growth only at the crack tip within the adhesive layer, rather than failure at a number of sites ahead of the main crack tip; consequently, the failure mode for the DCB specimen may differ from than in the butt joint specimen.

In contrast, a more sophisticated analysis could assume the existing of competing cohesive zones along the adhesive/adherend interfaces or within the adhesive of the square-wave geometry. Additionally, the adhesive could be modelled as an elastic (or visco elastic) solid. This alternative approach is in the same spirit as that of Pardoen et al. (2005) and of Suzuki et al. (2013, 2015), and could explore explicitly the effect of adhesive layer thickness, and square wave topology, upon macroscopic toughness. However, this alternative approach would require a number of additional assumptions, and material calibrations, on the constitutive response of the adhesive and on the mixed mode cohesive zone law for both interfacial and adhesive failure. Such an analysis is beyond the scope of the present study.

7. Appendix A: Use of the *J*-Integral to determine the cohesive zone law

As discussed in the Introduction, the traction versus separation law can be derived from the relationship between an elastic calculation of the energy release rate J and the crack tip opening displacement δ. Due to the large deformation before failure of the elastomeric adhesive, it is necessary to include the contribution of rotation of the substrates near the crack tip as a second term in the expression of the energy release rate (Högberg et al., 2007):

$$J = \frac{12}{EH^3}\left(\frac{Pa}{B}\right)^2 + \frac{P}{B}\phi \qquad (A.1)$$

where ϕ is the opening angle formed by the arms of the DCB specimen at the crack tip.

The opening displacement δ and angle φ are each measured from sequential photos of DCB specimens at the location a_o of the initial crack tip, see Figure A.1(a). The *J*-integral is

plotted as a function of δ in Figure A.1(b); it is seen that J increases monotonically to a steady-state value J_{ss}.

Very close to the crack tip, the J-integral is defined as

$$J = \int_0^{\delta_c} T(\delta)\, d\delta \qquad\qquad \text{(A.2)}$$

where δ_c is equal to the local displacement at which J_{ss} is reached. Due to the path-independence of J, the two preceding expressions are equal for a crack in an elastic solid. The traction acting across the interface follows directly from differentiation:

$$T(\delta) = \frac{dJ}{d\delta} \qquad\qquad \text{(A.3)}$$

This result implies a strong dependence of $T(\delta)$ on the form of the equation used to fit the $J(\delta)$ data. A detailed study is offered by Zhu and colleagues (Zhu et al., 2009), who obtained good results from a cubic polynomial fit. In the present work, a cubic polynomial equation is also adopted for $J(\delta)$.

Traction versus separation curves are calculated and compared to experimental data for tensile specimens in Figure A.1(c). The peak traction of the J-derived cohesive law is somewhat below the experimentally-measured value, and such a discrepancy is to be expected given the fact that (A.3) entails differentiation of an observed response involving both crack opening displacement and crack opening angle, recall (A.1).

The J-derived T-δ curve is characterised by a non-zero traction at zero displacement, implying an unbounded initial cohesive element stiffness. An unbounded element stiffness is impossible to implement in the finite element model. The highest possible stiffness is instead desirable, so that the energy under the traction versus separation curve remains relatively unchanged. A sensitivity study has been conducted to identify the highest stiffness which the model can handle without encountering numerical instabilities. Based on this sensitivity analysis, an element stiffness of 3 x 10^{10} Pa/m has been chosen.

The load versus displacement response of the DCB specimen is predicted by the finite element model using the J-derived cohesive zone law is presented in Figure A.1(d). The peak load of the cohesive zone model falls below the experimental value. Nevertheless, the cohesive zone model provides a reasonable fit. This method has been used by several researchers to obtain cohesive laws (Desai et al., 2015; Sørensen, 2002; Stigh et al., 2010; Zhu et al., 2009).

8. Acknowledgements

9. References

Alfano, G., 2006. On the influence of the shape of the interface law on the application of cohesive-zone models. Compos. Sci. Technol. 66, 723–730.

Alfano, M., Furgiuele, F., Leonardi, A., Maletta, C., Paulino, G.H., 2009. Mode I fracture of adhesive joints using tailored cohesive zone models, in: International Journal of Fracture. pp. 193–204. doi:10.1007/s10704-008-9293-4

Blackman, B.R.K., Hadavinia, H., Kinloch, A.J., Williams, J.G. 2003. The use of a cohesive zone model to study the fracture of fibre composites and adhesively-bonded joints, Int. J. Fracture, 119, 25-46.

Campilho, R.D.S.G., Banea, M.D., Neto, J.A.B.P., da Silva, L.F.M., 2013. Modelling adhesive joints with cohesive zone models: effect of the cohesive law shape of the adhesive layer. Int. J. Adhes. Adhes. 44, 48–56. doi:10.1016/j.ijadhadh.2013.02.006

Cooper, V., Ivankovic, A., Karac, A., McAuliffe, D., Murphy, N. 2012. Effects of bondgap thickness on the fracture of nano-toughened epoxy adhesive joints. Polymer, 53, 5540-5553.

Cordisco, F.A., Zavattieri, P.D., Hector, L.G., Carlson, B.E., 2016. Mode I fracture along adhesively bonded sinusoidal interfaces. Int. J. Solids Struct. 83, 45–64. doi:10.1016/j.ijsolstr.2015.12.028

Desai, C.K., Basu, S., Parameswaran, V., 2015. Determination of Traction Separation Law for Interfacial Failure in Adhesive Joints at Different Loading Rates. J. Adhes. 8464, 150527102921008. doi:10.1080/00218464.2015.1046986

Elices, M., Guinea, G.V., Gómez, J., Planas, J., 2002. The cohesive zone model: advantages, limitations and challenges. Eng. Fract. Mech. 69, 137–163. doi:10.1016/S0013-

7944(01)00083-2

Ferracin, T., Landis, C.M., Delannay, F., Pardoen, T., 2003. On the determination of the cohesive zone properties of an adhesive layer from the analysis of the wedge-peel test. Int. J. Solids Structs., 40, 2889-2904.

Georgiou, I., H. Hadavinia, H., Ivankovic, A., Kinloch, A.J., Tropsa, V., Williams, J.G., 2003. Cohesive zone models and the plastically deforming peel test, J. of Adhesion, 79, 239-265, DOI: 10.1080/00218460309555

Gustafson, P.A., Waas, A.M., 2009. The influence of adhesive constitutive parameters in cohesive zone finite element models of adhesively bonded joints. Int. J. Solids Struct. 46, 2201–2215. doi:10.1016/j.ijsolstr.2008.11.016

Hikosaka, Y., Matsuzaki, R., Todoroki, A., Mizutani, Y., 2013. Crack growth analysis of a composite/adhesive interface toughened by in-mold surface preparation. eXPRESS Polymer Letters, 7, 293-303.

Högberg, J.L., Sørensen, B.F., Stigh, U., 2007. Constitutive behaviour of mixed mode loaded adhesive layer. Int. J. Solids Struct. 44, 8335–8354. doi:10.1016/j.ijsolstr.2007.06.014.

Ivankovic, A., Pandya, K.C., Williams, J.G., 2004. Crack growth predictions in polyethylene using measured traction–separation curves. Eng. Fract. Mech. 71, 657–668. doi:10.1016/S0013-7944(03)00030-4

Kim, W.-S., Yun, I.-H., Lee, J.-J., Jung, H.-T., 2010. Evaluation of mechanical interlock effect on adhesion strength of polymer-metal interfaces using micro-patterned surface topography. Int. J. of Adhesion and Adh., 30 (6), 408-417.

Karac, A, Blackman, B.R.K., Cooper, V., Kinloch, A.J., Sanchez, S.R., Teo, W.S., Ivankovic, A. 2011, Modelling the fracture behaviour of adhesively bonded joints as a function of test rate, Engineering Fracture Mechanics, 78, 973-989.

Li, S., Thouless, M.D., Waas, A.M., Schroeder, J.A., Zavattieri, P.D., 2005. Use of mode-I cohesive-zone models to describe the fracture of an adhesively-bonded polymer-matrix composite. Compos. Sci. Technol. 65, 281–293. doi:10.1016/j.compscitech.2004.07.009

Maloney, K.J., Fleck, N.A., 2017. Damage tolerance of a micro-architected adhesive joint. Int. J. Solids Struct., in press, doi:/10.1016/j.ijsolstr.2017.06.010

Martiny, Ph., Lani, F., Kinloch, A.J., Pardoen, T., 2008. Numerical analysis of the energy contributions in peel tests: a steady-state multilevel finite element approach. Int. J.

Adhesion and Adh., 28, 222-236.

Matsuzaki, R., Suzuki, T., 2010. Surface modification by nanoimprint lithography for improvement of the joint strength of composites. J. Solid Mech. and Mat. Eng., 4, 963-973.

Mohammed, I., Liechti, K.M., 2000. Cohesive zone modeling of crack nucleation at bimaterial corners. J. Mech. Phys. Solids 48, 735–764. doi:10.1016/S0022-5096(99)00052-6

Pardoen, T., Ferracin, T., Landis, C.M., Delannay, F., 2005. Constraint effects in adhesive joint fracture. J. Mech. Phys. Solids 53, 1951-1983.

Park, K., Paulino, G.H., 2013. Cohesive Zone Models: A Critical Review of Traction-Separation Relationships Across Fracture Surfaces. Appl. Mech. Rev. 64, 60802. doi:10.1115/1.4023110

Salomonsson, K., Andersson, T., 2008. Modeling and parameter calibration of an adhesive layer at the meso level. Mech. Mater. 40, 48–65. doi:http://dx.doi.org/10.1016/j.mechmat.2007.06.004

Shet, C., Chandra, N., 2002. Analysis of Energy Balance When Using Cohesive Zone Models to Simulate Fracture Processes. J. Eng. Mater. Technol. 124, 440. doi:10.1115/1.1494093

Sørensen, B.F., 2002. Cohesive law and notch sensitivity of adhesive joints. Acta Mater. 50, 1053–1061. doi:10.1016/S1359-6454(01)00404-9

Stigh, U., Alfredsson, K.S., Andersson, T., Biel, A., Carlberger, T., Salomonsson, K., 2010. Some aspects of cohesive models and modelling with special application to strength of adhesive layers. Int. J. Fract. 165, 149–162. doi:10.1007/s10704-010-9458-9.

Suzuki, T., Matsuzaki, R., Todoroki, A., Mizutani, Y., 2013. Crack growth analysis of a composite/adhesive interface toughened by in-mold surface preparation. Int. J. of Adhesion and Adh., 42, 36-43.

Suzuki, T., Matsuzaki, R., Todoroki, A., Mizutani, Y., 2015. Prediction of the macroscopic fracture toughness of a composite/adhesive interface with periodic surface microstructures. Int. J. of Adhesion and Adh., 60, 16-22.

Tvergaard, V., Hutchinson, J.W., 1992. The relation between crack growth resistance and fracture process parameters in elastic-plastic solids. J. Mech. Phys. Solids 40, 1377–

1397. doi:10.1016/0022-5096(92)90020-3

Tvergaard, V., Hutchinson, J.W., 1994. Toughness of an interface along a thin ductile layer joining elastic solids. Philos. Mag. A 70, 641–656.

Tvergaard, V., Hutchinson, J.W., 1996. On the toughness of ductile adhesive joints. J. Mech. Phys. Solids 44, 789–800.

Yang, Q., Cox, B., 2005. Cohesive models for damage evolution in laminated composites. Int. J. Fract. 133, 107–137. doi:10.1007/s10704-005-4729-6

Yang, Q.D., Thouless, M.D., Ward S.M., 1999. Numerical simulation of adhesively-bonded beams failing with extensive plastic deformation. J. Mech. Phys. Solids 47, 1337-1353.

Yang, Q.D., Thouless, M.D., 2001. Mixed-mode fracture analyses of plastically-deforming adhesive joints. Int. J. Fract. 110, 175–187.

Yukimoto, Y., Matsuzaki, R., Todoroki, A., 2014. Mode II interfacial fracture toughness of composite/adhesive interfaces obtained by in mold surface modification. Int. J. of Adhesion and Adh., 50, 191-198.

Zavattieri, P.D., Hector, L.G., Bower, A.F., 2007. Determination of the effective mode-I toughness of a sinusoidal interface between two elastic solids. Int. J. Fract. 145, 167–180. doi:10.1007/s10704-007-9109-y

Zhu, Y., Liechti, K.M., Ravi-Chandar, K., 2009. Direct extraction of rate-dependent traction–separation laws for polyurea/steel interfaces. Int. J. Solids Struct. 46, 31–51. doi:10.1016/j.ijsolstr.2008.08.019

10. Tables

Table 1: Parameters of cohesive laws for finite element simulations of DCB joints.

A (mm)	0	2.5	10	20
K (GPa/m)	20	9	9	12
T_0 (MPa)	1.0	1.0	1.0	1.2

11. Figure Captions

Figure 1: (a) Geometry of experimental double-cantilever beam (DCB) adhesive joint specimens, with square-wave interfaces. (b) Parameters of the square-wave interface.

Figure 2: Uniaxial tension response of silyl-modified polymer (SMP) adhesive at three strain rates, from dogbone specimens.

Figure 3: (a) Load versus displacement response of a planar DCB joint ($A = 0$ mm; $t = 1.1$ mm). At three instances (as indicated), a shim was inserted and the joint was removed from the load frame and scanned using computed tomography (CT). (b) Three CT images of the x-z mid-plane in the adhesive layer, equidistant from each substrate. (c) Fracture surface to show voiding from filler particles within the adhesive.

Figure 4: The tensile responses of (a) DCB joints and (b) butt joints with square-wave amplitude A = 0 (corresponding to planar interfaces), 2.5, 10, and 20 mm. (c) Energy dissipation of butt joints and double-cantilever beam joints as a function of square-wave amplitude A. Adhesive layer thickness t = 1.1 mm.

Figure 5: Images of failure sequences for a square-wave DCB joint and a tensile butt joint, A=20 mm, t= 1.1 mm. The images are compared at similar values of local separation, and stages of damage (i) to (v) are indicated for the butt joint.

Figure 6: Experimental response of a tensile butt joint. The solid line is the experimental response and the dotted lines are constant values of damage variable D. Critical traction T_0, corresponding to the onset of damage, and peak traction T_{max} are noted.

Figure 7: (a) The response of the double-cantilever beam finite element model (dotted lines) overlaid on experimental results (solid lines) for square-wave joints of four square-wave amplitudes $0 \leq A \leq 20$ mm. Adhesive layer thickness t = 1.1 mm, beam height H = 25.4 mm. (b) The responses of the finite element model with adjusted beam height H_{eq} are compared to experimental results.

Figure A.1: (a) Crack tip opening displacement δ and opening angle φ measured from photos at the location of the initial crack tip (a_o = 30 mm) for a planar DCB joint with adhesive layer thickness $t = 1.1 \pm 0.1$ mm. (b) Results of an elastic calculation for the energy release rate J as a function of crack tip opening displacement δ. The hollow data points indicate that crack extension has occurred. (c) Comparison between traction versus separation curves as calculated from $J(\delta)$, and as measured directly from the tensile response of a butt joint. (d) Load versus displacement response of the planar DCB joint by measurement and by finite element model.
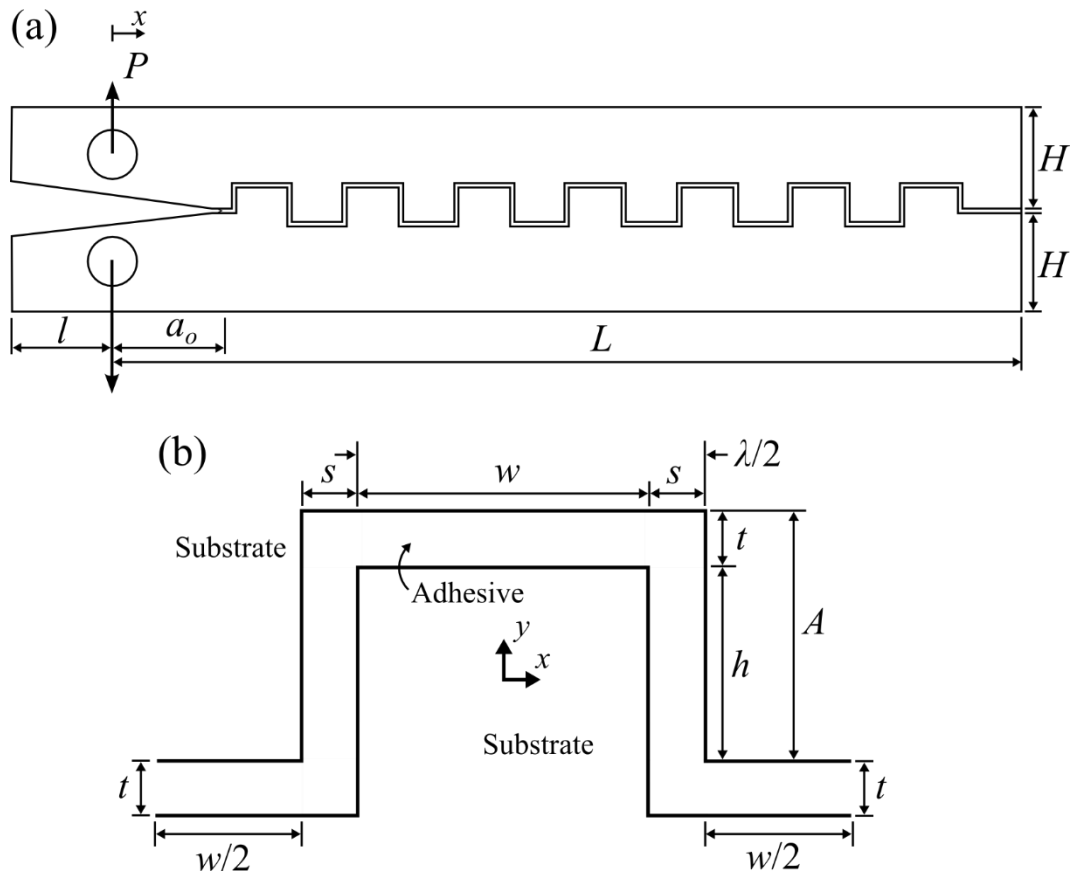
12. Figures

Figure 1: (a) Geometry of experimental double-cantilever beam (DCB) adhesive joint specimens, with square-wave interfaces. (b) Parameters of the square-wave interface.
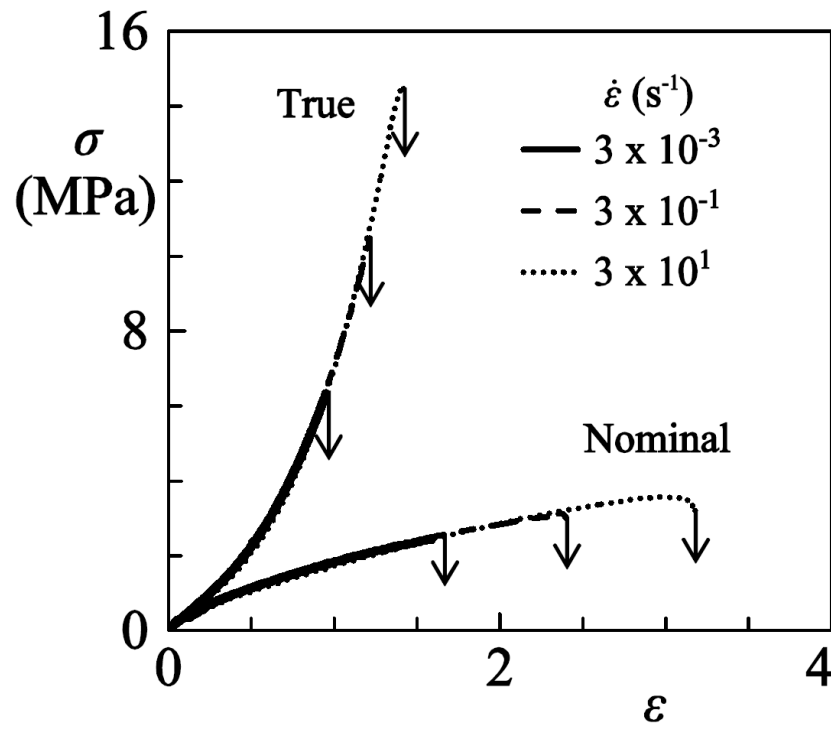
Figure 2: Uniaxial tension response of silyl-modified polymer (SMP) adhesive at three strain rates, from dogbone specimens.
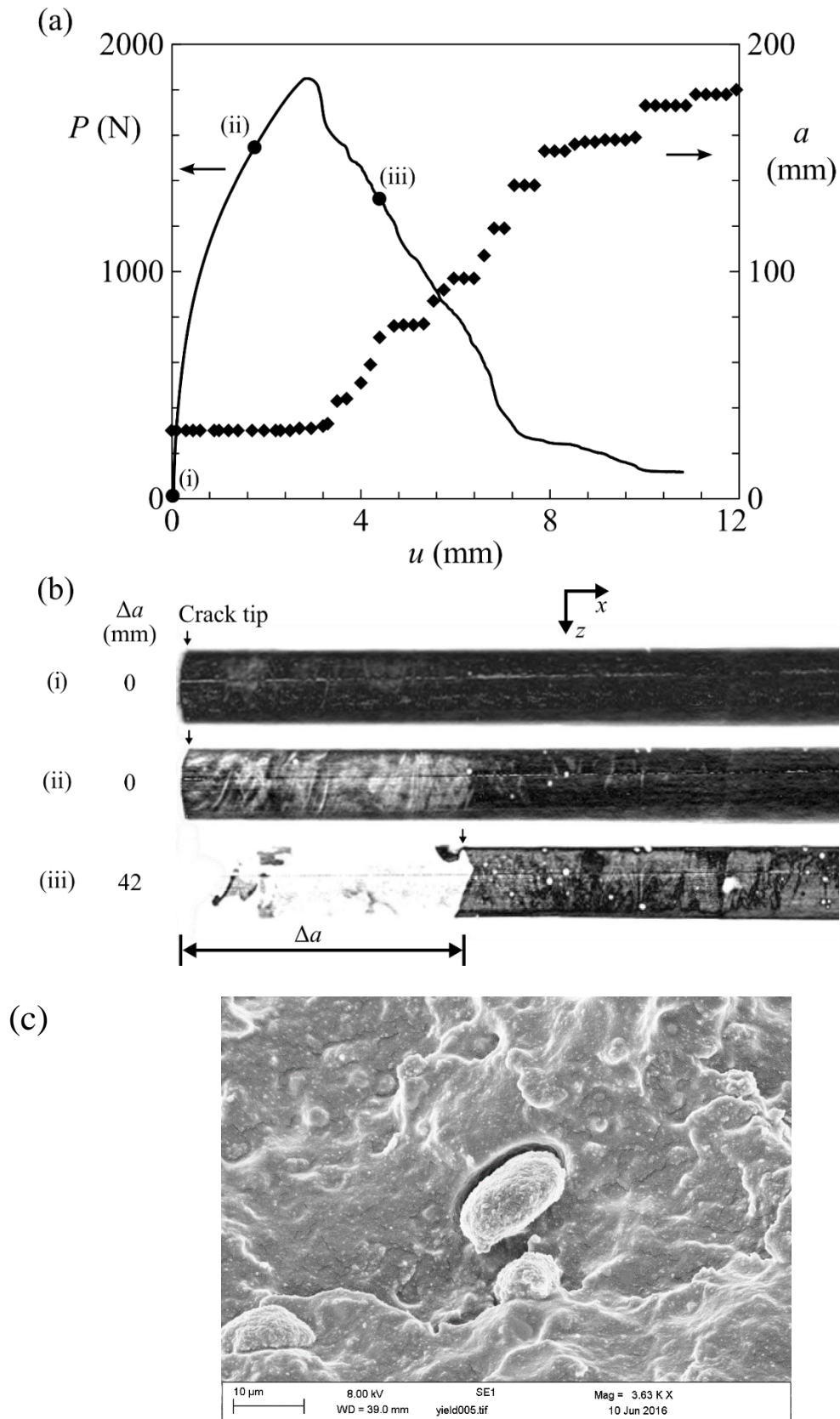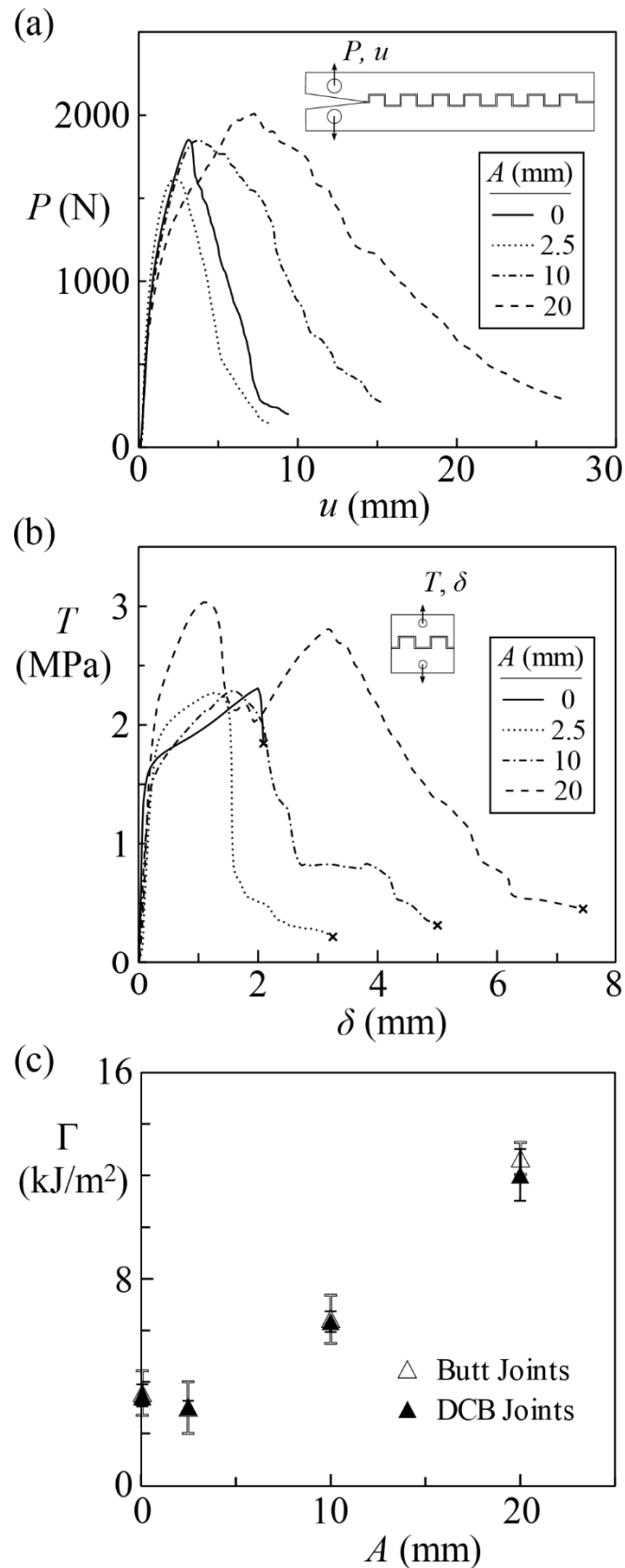
Figure 3: (a) Load versus displacement response of a planar DCB joint ($A = 0$ mm; $t = 1.1$ mm). At three instances (as indicated), a shim was inserted and the joint was removed from the load frame and scanned using computed tomography (CT). (b) Three CT images of the x-z mid-plane in the adhesive layer, equidistant from each substrate. (c) Fracture surface to show voiding from filler particles within the adhesive.

Figure 4: The tensile responses of (a) DCB joints and (b) butt joints with square-wave amplitude $A = 0$ (corresponding to planar interfaces), 2.5, 10, and 20 mm. (c) Energy dissipation of butt joints and double-cantilever beam joints as a function of square-wave amplitude A. Adhesive layer thickness $t = 1.1$ mm.
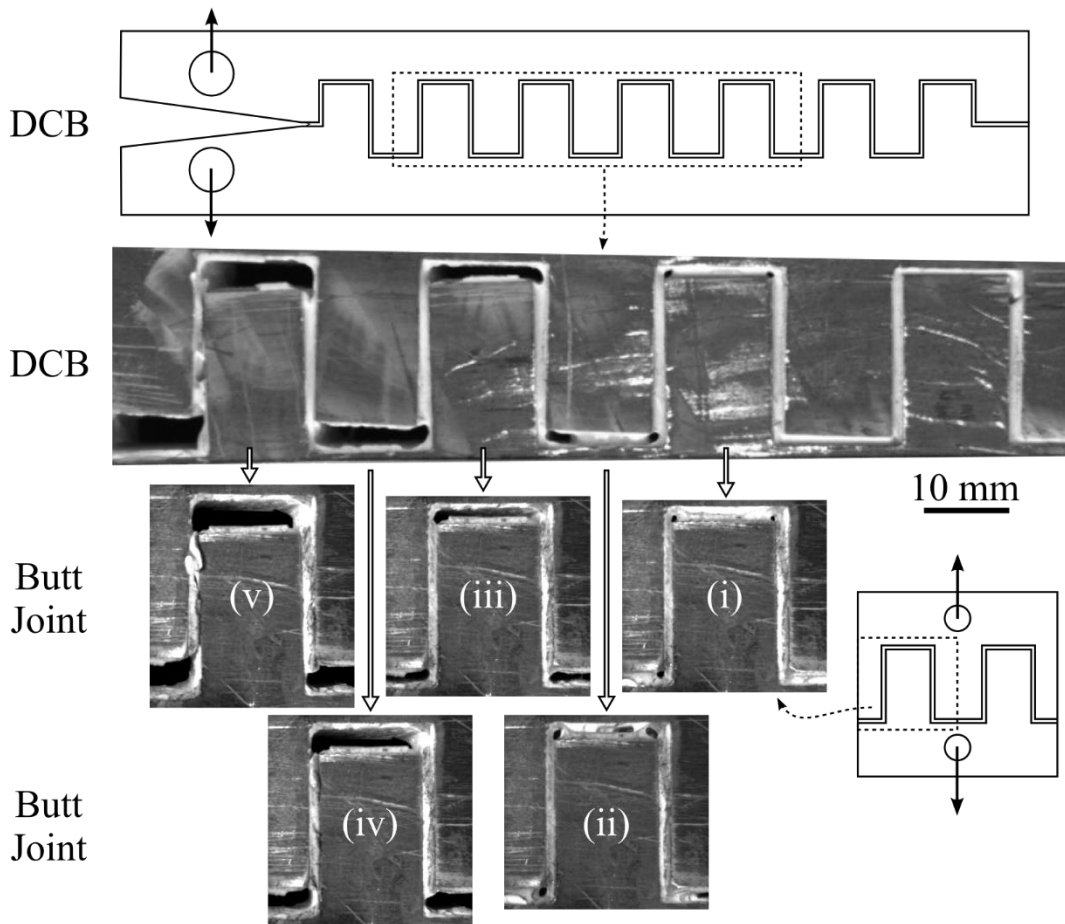
Figure 5: Images of failure sequences for a square-wave DCB joint and a tensile butt joint, A=20 mm, t= 1.1 mm. The images are compared at similar values of local separation, and stages of damage (i) to (v) are indicated for the butt joint.
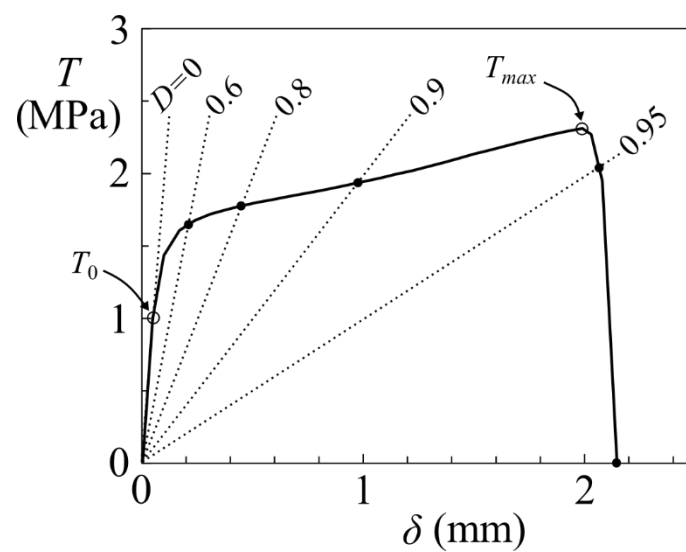

Figure 6: Experimental response of a tensile butt joint. The solid line is the experimental response and the dotted lines are constant values of damage variable D. Critical traction T_0, corresponding to the onset of damage, and peak traction T_{max} are noted.
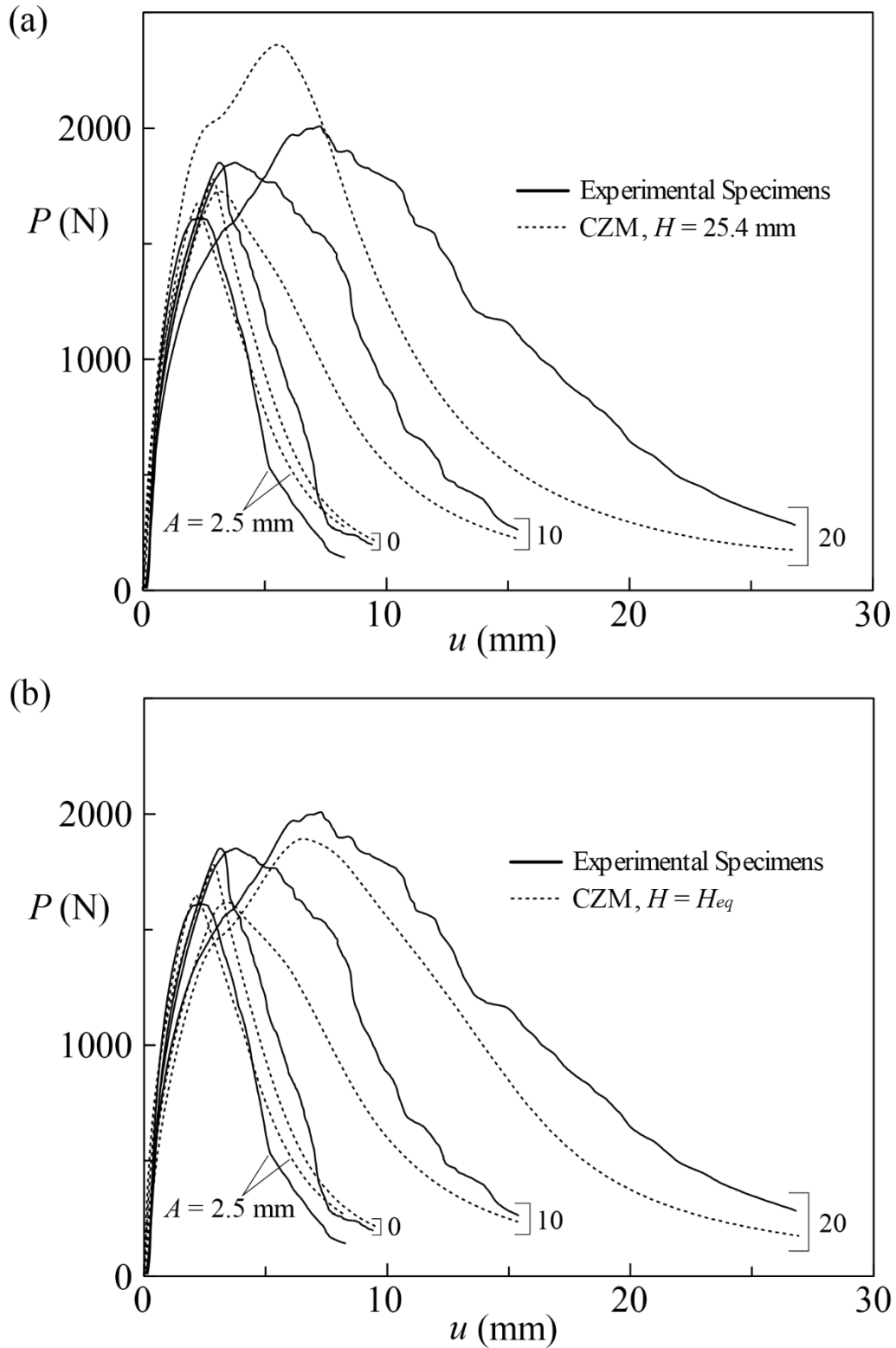
Figure 7: (a) The response of the double-cantilever beam finite element model (dotted lines) overlaid on experimental results (solid lines) for square-wave joints of four square-wave amplitudes $0 \leq A \leq 20$ mm. Adhesive layer thickness $t = 1.1$ mm, beam height $H = 25.4$ mm. (b) The responses of the finite element model with adjusted beam height H_{eq} are compared to experimental results.
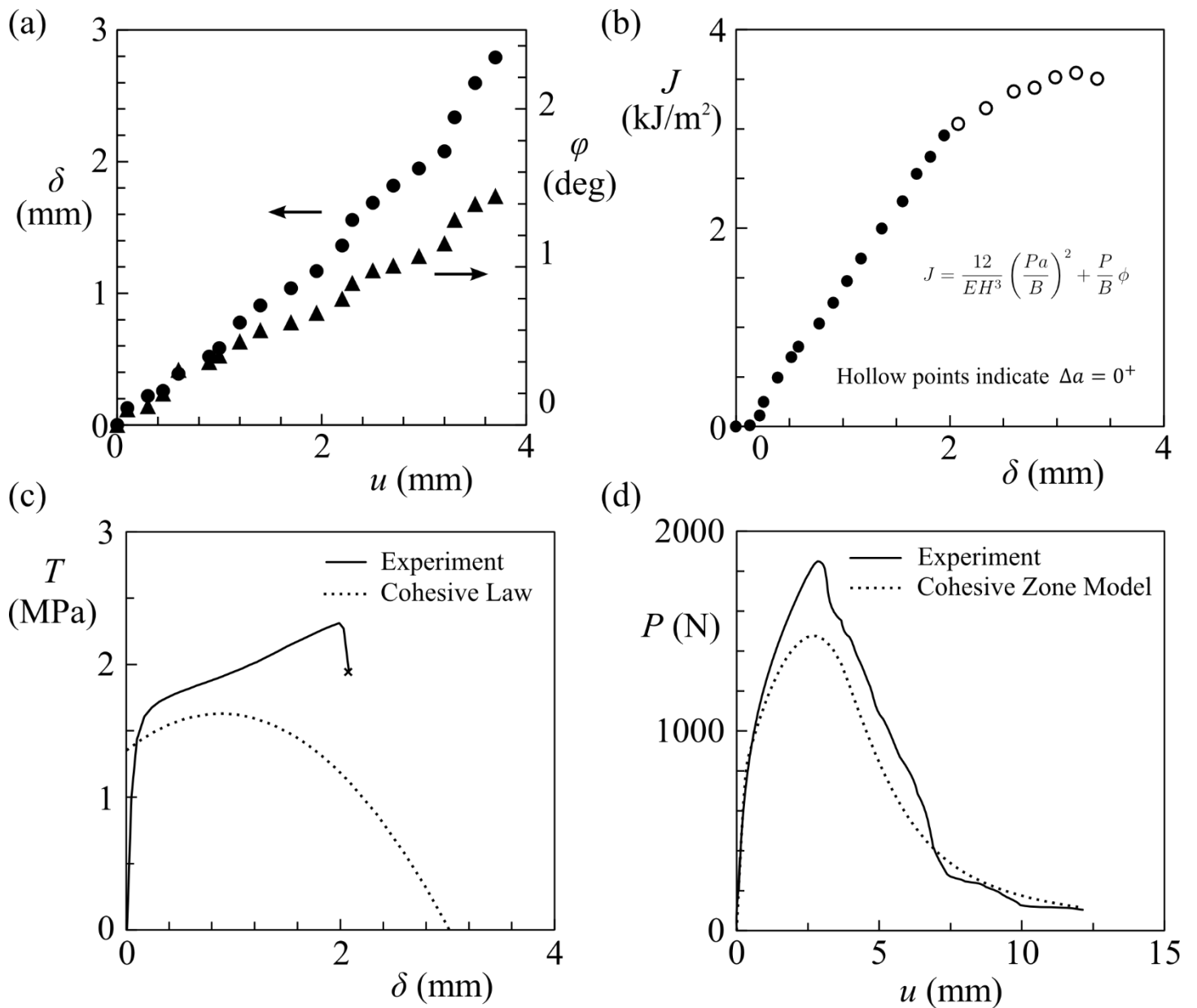
Figure A.1: (a) Crack tip opening displacement δ and opening angle φ measured from photos at the location of the initial crack tip ($a_o = 30$ mm) for a planar DCB joint with adhesive layer thickness $t = 1.1 \pm 0.1$ mm. (b) Results of an elastic calculation for the energy release rate J as a function of crack tip opening displacement δ. The hollow data points indicate that crack extension has occurred. (c) Comparison between traction versus separation curves as calculated from $J(\delta)$, and as measured directly from the tensile response of a butt joint. (d) Load versus displacement response of the planar DCB joint by measurement and by finite element model.